Publications of the Astronomical Society of Australia (2020), **37**, e025, 14 pages
doi:10.1017/pasa.2020.16

CAMBRIDGE UNIVERSITY PRESS

Research Paper

Understanding galaxy formation and evolution through an all-sky submillimetre spectroscopic survey

Mattia Negrello [1], Matteo Bonato [2,3], Zhen-Yi Cai [4,5], Helmut Dannerbauer [6,7], Gianfranco De Zotti [3], Jacques Delabrouille [8,9] and Douglas Scott [10]

[1]School of Physics and Astronomy, Cardiff University, The Parade, Cardiff CF24 3AA, UK, [2]INAF-Istituto di Radioastronomia, and Italian ALMA Regional Centre, Bologna, Italy, [3]INAF, Osservatorio Astronomico di Padova, Vicolo Osservatorio 5, I-35122 Padova, Italy, [4]CAS Key Laboratory for Research in Galaxies and Cosmology, Department of Astronomy, University of Science and Technology of China, Hefei 230026, China, [5]School of Astronomy and Space Science, University of Science and Technology of China, Hefei 230026, China, [6]Instituto de Astrofísica de Canarias (IAC), E-38205 La Laguna, Tenerife, Spain, [7]Universidad de La Laguna, Dpto. Astrofísica, E-38206 La Laguna, Tenerife, Spain, [8]Laboratoire Astroparticule et Cosmologie, CNRS/IN2P3, 75205 Paris Cedex 13, France, [9]Département d'Astrophysique, CEA Saclay DSM/Irfu, 91191 Gif-sur-Yvette France and [10]Department of Physics & Astronomy, University of British Columbia, Vancouver, Canada

Abstract

We illustrate the extraordinary discovery potential for extragalactic astrophysics of a far-infrared/submillimetre (far-IR/submm) all-sky spectroscopic survey with a 3-m-class space telescope. Spectroscopy provides a three-dimensional view of the Universe and allows us to take full advantage of the sensitivity of present-day instrumentation, close to fundamental limits, overcoming the spatial confusion that affects broadband far-IR/submm surveys. A space telescope of the 3-m class (which has already been described in recent papers) will detect emission lines powered by star formation in galaxies out to $z \simeq 8$. It will specifically provide measurements of spectroscopic redshifts, star-formation rates (SFRs), dust masses, and metal content for millions of galaxies at the peak epoch of cosmic star formation and of hundreds of them at the epoch of reionisation. Many of these star-forming galaxies will be strongly lensed; the brightness amplification and stretching of their sizes will make it possible to investigate (by means of follow-up observations with high-resolution instruments like ALMA, *JWST*, and SKA) their internal structure and dynamics on the scales of giant molecular clouds (40–100 pc). This will provide direct information on the physics driving the evolution of star-forming galaxies. Furthermore, the arcmin resolution of the telescope at submm wavelengths is ideal for detecting the cores of galaxy proto-clusters, out to the epoch of reionisation. Due to the integrated emission of member galaxies, such objects (as well as strongly lensed sources) will dominate at the highest apparent far-IR luminosities. Tens of millions of these galaxy-clusters-in-formation will be detected at $z \simeq 2$–3, with a tail extending out to $z \simeq 7$, and thousands of detections at $6 < z < 7$. Their study will allow us to track the growth of the most massive halos well beyond what is possible with classical cluster surveys (mostly limited to $z \lesssim 1.5$–2), tracing the history of star formation in dense environments and teaching us how star formation and galaxy-cluster formation are related across all epochs. The obscured cosmic SFR density of the Universe will thereby be constrained. Such a survey will overcome the current lack of spectroscopic redshifts of dusty star-forming galaxies and galaxy proto-clusters, representing a quantum leap in far-IR/submm extragalactic astrophysics.

Keywords: galaxies: clusters: general – galaxies: evolution – galaxies: high-redshift – galaxies: luminosity function – submillimetre: galaxies

(Received 9 January 2020; revised 11 March 2020; accepted 12 April 2020)

1. Introduction

The L-class space mission proposed by Delabrouille et al. (2019) will have a tremendous impact on our understanding of the Universe and on many branches of astrophysics. The project features two instruments at the focus of a 3-m-class, cold (8 K) telescope: (i) a broad-band, multi-frequency, polarimetric imager operating over the 20–800 GHz frequency range that would map the cosmic microwave background (CMB) at high sensitivity, as well as the thermal and kinetic Sunyaev–Zeldovich (SZ) effects and the galactic and extragalactic continuum emissions; and (ii) a moderate spectral resolution ($R \simeq 300$) filter-bank spectrometer covering the 100–1 000 GHz band. These two instruments would comprise tens of thousands of millimetre (mm) and submillimetre (submm) detectors cooled to sub-kelvin temperatures for sky-background-limited performance.

A set of Fourier-transform spectrometers (FTSs), covering the full 10–2 000 GHz band with spectral resolution ranging from 2.5 to 60 GHz, could also be hosted on the same platform. This instrument would carry out absolute measurements of the CMB spectrum with a sensitivity 4 to 5 orders of magnitude better than *COBE*-FIRAS.

An overview of the scientific goals of the project has been presented by Delabrouille et al. (2019), while other white papers related to the ESA 'Voyage 2050'[a] call have elaborated on specific science cases. Basu et al. (2019) dealt with the use of the

Author for correspondence: Helmut Dannerbauer and Gianfranco De Zotti, E-mails: helmut@iac.es; gianfranco.dezotti@inaf.it

Cite this article: Negrello M, Bonato M, Cai Z-Y, Dannerbauer H, De Zotti G, Delabrouille J and Scott D. (2020) Understanding galaxy formation and evolution through an all-sky submillimetre spectroscopic survey. *Publications of the Astronomical Society of Australia* **37**, e025, 1–14. https://doi.org/10.1017/pasa.2020.16

[a]Call by ESA in order to prepare the long-term plan of the ESA science programme.

CMB as a 'back-light', illuminating the entire observable Universe, thus allowing us to obtain a complete census of the total mass, gas, and stellar contents of the Cosmos across time. Silva et al. (2019) looked into the promise of mapping the intensity of the many mm/submm/far-infrared (far-IR) lines detectable by the proposed instrument to address several open questions relating to the reionisation process, galaxy evolution, the cosmic infrared background (CIB), and fundamental cosmology. Additionally, the unique information on the thermal history of the Universe provided by absolute spectral measurements has been highlighted by Chluba et al. (2019).

Here we argue that the high-sensitivity spectroscopic and imaging surveys carried out by this space mission would revolutionise our understanding of galaxy formation and evolution and of the growth of large-scale structure back to the epoch of reionisation.

For more than 20 yr, surveys at far-IR to submm wavelengths have played a key role in our understanding of early galaxy and active galactic nuclei (AGN) evolution (for reviews, see Lutz 2014; Casey, Narayanan, & Cooray 2014). The SCUBA discovery of a copious population of submm-bright galaxies (Smail, Ivison, & Blain 1997; Barger et al. 1998; Hughes et al. 1998), shown to be at high redshifts (Ivison et al. 1998; Barger et al. 1999; Swinbank et al. 2004; Chapman et al. 2005; Pope et al. 2006), strongly challenged the widely accepted pictures of galaxy formation and evolution. In fact, simple merger-driven models dramatically underpredicted the abundance of bright submm galaxies and the CIB intensity, using standard assumptions for the stellar Initial Mass Function (IMF) and for the dust temperature distribution (see, e.g., Kaviani, Haehnelt, & Kauffmann 2003; Baugh et al. 2005; Niemi et al. 2012; Somerville et al. 2012; Gruppioni et al. 2015).

The submm spectral region is exceptionally well suited to provide access to the dust-enshrouded most active star-formation phases of young galaxies in the high-z Universe. This is because, for a large redshift range, submm wavelengths (in the observer's frame) are in the Rayleigh–Jeans region of the dust emission spectrum, where the flux density scales as $S_\nu \propto \nu^{2+\beta}$, the dust emissivity index, β, generally being in the range 1.5–2. The corresponding so-called 'negative K-correction' largely compensates, and may even slightly over-compensate the decrease of the flux density with increasing luminosity distance (Franceschini et al. 1991; Blain & Longair 1993), providing roughly luminosity-limited samples. Thus, dusty star-forming galaxies (DSFGs) can be detected out to $z \simeq 8$–10 without the need for extreme sensitivities.

Ground-based observations at submm wavelengths are severely limited by water vapour in the atmosphere, leaving only a few windows even in the driest sites; hence the need for space missions. The *Herschel* observatory surveyed about 1300 deg^2 of the extragalactic sky, primarily thanks to the *Herschel* Astrophysical Terahertz Large Area Survey (H-ATLAS; Eales et al. 2010), to the *Herschel* Multi-tiered Extragalactic Survey (HerMES; Oliver et al. 2012) and to the *Herschel* Stripe 82 Survey (HerS; Viero et al. 2014), which covered 660, 380, and 79 deg^2, respectively.

The *Herschel* surveys with the Spectral and Photometric Imaging Receiver (SPIRE), operating at 250, 350, and 500 μm, were confusion limited at rms values of 5.8, 6.3, and 6.8 mJy beam^{-1}, respectively (Nguyen et al. 2010). Source confusion does not allow us to take full advantage of the sensitivity (which is close to fundamental limits) of present-day detectors. The problem can be overcome using larger telescopes, thereby providing better angular resolution, but this implies higher costs and limits on the total area that can be surveyed.

An interesting alternative is offered by spectroscopy. Adding the third dimension essentially removes the confusion problem. The reason for this is clear—moderate resolution spectroscopy with, say, $R \equiv \nu/\Delta\nu = 300$, apportions sources detected with broadband photometry with, e.g., $\Delta\nu/\nu = 0.3$ to 100 almost equally populated narrow redshift bins, each with much lower, generally negligible, confusion noise. Precisely how to most efficiently disentangle the spectra of sources from spatially confused (but spectrally unconfused) data cubes remains an open research question (see discussion in Appendix E.1 of Meixner et al. 2019), but it is clear that in principle the information is there to extract.

The relatively large beam sizes of submm telescopes have another serious drawback: the difficulty in identifying multi-frequency counterparts to measure their spectroscopic redshifts. High-z DSFGs are generally very faint at other wavelengths, such as in the optical or near-IR that do not benefit from the negative K-correction (e.g., Dannerbauer et al. 2002, 2004; Dunlop et al. 2004; Pope et al. 2005; Younger et al. 2007; Dannerbauer, Walter, & Morrison 2008; Walter et al., 2012). The surface densities of faint optical/near-IR sources are very high, making the identification of the correct counterpart difficult. Deep radio observations help a lot in this respect (e.g., Ivison et al. 2002; Dannerbauer et al. 2004; Biggs, Younger, & Ivison 2010). Acquiring spectroscopic redshifts through follow-up studies with mm/submm telescopes is a time-consuming process, impractical for very large galaxy samples. Although far-IR/submm surveys have discovered tens of thousands of distant DSFGs, the number of measured spectroscopic redshifts is still not more than a few hundreds (e.g., Casey et al. 2012a, 2012b, Bothwell et al. 2013; Weiss et al. 2013; Danielson et al. 2017; Fudamoto et al. 2017; Zhang et al. 2018a; Neri et al. 2020). Thus, only coarse far-IR-photometric redshift estimates are generally possible for samples of several hundred to thousands of high-z IR-luminous objects.

A moderate spectral resolution ($R \simeq 300$) filter-bank spectrometer at the focus of a 3-m-class telescope will yield exciting results in several areas. For definiteness, we consider a cold (8 K) telescope with a 3.5-m aperture primary (the same size as *Herschel*) with a secondary mirror and cold stop at 4 K and 20 dB edge taper, as proposed by Delabrouille et al. (2019).

This instrument would deliver unique results in many branches of astrophysics. Here we will specifically discuss its potential for

- investigating the physical processes driving the assembly of galaxies and exploring the evolution of their metal and dust content out to $z \simeq 8$;
- measuring the early growth (to $z \simeq 7$) of large-scale structures (i.e., galaxy proto-clusters), when their member galaxies were actively star forming, and when the hot gas, making them detectable in X-rays or via the SZ effect was not necessarily in place yet.

The plan of the paper is the following. In Section 2, we give the 5σ line-detection limits of the proposed instrument and the corresponding minimum star-formation rate (SFR), as a function of redshift, detectable in lines for the average relationship between line luminosity and SFR. In Section 3, we briefly describe our reference model and present predictions of the redshift distributions of galaxies detected in lines and of the cumulative SFR functions at various redshifts, out to $z \simeq 8$. In Sections 4 and 5, we highlight examples of the new science enabled by these data on strongly gravitationally lensed and unlensed galaxies. In Section 6,

https://doi.org/10.1017/pasa.2020.16 Published online by Cambridge University Press

we compare the proposed survey with those of other forthcoming or planned instruments. Section 7 discusses the potential of this project for reconstructing the full history of the most massive virialised structures in the Universe, namely galaxy clusters. Section 8 presents a comparison with cluster surveys in other wavebands. Finally, Section 9 summarises our main conclusions.

We adopt a flat ΛCDM cosmology with the latest values of the parameters derived from Planck CMB power spectra: $H_0 = 67.4\,\mathrm{km\,s^{-1}\,Mpc^{-1}}$; and $\Omega_\mathrm{m} = 0.315$ (Planck Collaboration VI 2018).

2. Line-detection limits

Table 1 shows the estimated sensitivity and the 5σ point source and line-detection limits at a set of frequencies for a 2-yr survey of 90% of the sky with 64 polarised channelisers, covering the frequency range 100–1000 GHz with $R = 300$, using close to background limited MKID detectors (we assume a conservative 30% optical efficiency, and instrumental noise matching the sky background noise). A 6-month duration survey of 5% sky is also being considered; it goes deeper by a factor of approximately $\sqrt{5}$.

Exploiting observations, mostly from *Spitzer* and *Herschel*, Bonato et al. (2019) reported tight correlations between the main mid-IR-to-submm lines from neutral or ionised atomic gas and from molecular gas and the total IR luminosity, L_IR (conventionally defined over 8–1 000 μm), of dust heated by newly formed stars. The brightest lines detectable in the frequency range considered here are [NII] 205.18 μm, [CI] 170.42 μm, [CII] 157.7 μm, [OIII] 88.36 μm, [OI] 63.18 μm, and [OIII] 51.81 μm.

The line–L_IR relations obtained by Bonato et al. (2019) are based on observations of dusty galaxies, for which the unabsorbed fraction of the emission from young stars is small, so that L_IR is a measure of the total SFR. One might wonder whether the line luminosities are primarily related to L_IR or to the SFR, and an answer was provided by De Looze et al. (2014). For their sample of low-metallicity galaxies with moderate dust emission, they found that [OIII] 88.36 μm and [OI] 63.18 μm are good probes of the SFR measured through a composite tracer (*GALEX* FUV + *Spitzer*-MIPS 24 μm luminosity). The case is less clear for [CII] 157.7 μm; however, the [CII] emission in star-forming galaxies primarily arises from photo-dissociation regions (PDRs; Stacey et al. 2010), although it can also come from the partly ionised interstellar medium (e.g., Sutter 2019). Since PDRs are heated by the UV radiation emitted by young stars, [CII] has also been used as a measure of the SFR (e.g., Carniani et al. 2018). The [CII] luminosities of the $z \simeq 6.8$ galaxies without detected far-IR emission, observed by Smit et al. (2018), were found to be good SFR estimators. Schaerer et al. (2020) reported no or weak evolution of the [CII]–SFR relation over the last 13 Gyr, i.e. up to $z \sim 8$.

Based on these results, following Bonato et al. (2019), we assume that the luminosity of far-IR fine-structure lines primarily correlates with the SFR. Thus, the relations derived by Bonato et al. (2019) allow us to estimate the values of SFR as a function of z corresponding to the 5σ line-detection limits listed in Table 1. The results are shown in Figure 1, where the solid black line refers to the survey of 90% of the sky (the 'all-sky' survey), while the dotted blue line refers to the deep survey of 5% of the sky. At each redshift, we have computed the minimum SFR detectable in the various lines and taken the smallest one.

Our calculations assume that the lines are unresolved at $R = 300$, corresponding to line widths of $1,000\,\mathrm{km\,s^{-1}}$. This is almost always the case for individual galaxies. The spectroscopy of 15 H-ATLAS galaxies at $2.08 < z < 4.05$ obtained by Neri et al. (2020) with the IRAM NOrthern Extended Millimetre Array (NOEMA) yielded line widths (FWHM) between 150 and 1 100 $\mathrm{km\,s^{-1}}$ (mean $700 \pm 300\,\mathrm{km\,s^{-1}}$, median $800\,\mathrm{km\,s^{-1}}$). The [CII] 157.7 μm observations by Gullberg et al. (2015) of 16 spectrally resolved strongly lensed star-forming galaxies at $3.0 < z < 5.7$ yielded line FWHMs ranging from 198 ± 34 to $800 \pm 200\,\mathrm{km\,s^{-1}}$ with a median of $\simeq 541 \pm 110\,\mathrm{km\,s^{-1}}$. Nesvadba et al. (2019) measured the FWHMs of the [OI] 370.42 μm and 609.14 μm lines in the range from 220 ± 21 to $639 \pm 100\,\mathrm{km\,s^{-1}}$ (median $475\,\mathrm{km\,s^{-1}}$) for 11 strongly lensed submm galaxies detected by *Planck*. Similar values (from 220 ± 50 to $770 \pm 80\,\mathrm{km\,s^{-1}}$, median $370\,\mathrm{km\,s^{-1}}$) were measured by Cooke et al. (2018) for 10 serendipitous [CII] 157.7 μm emitters at $z \sim 4.5$.

A somewhat lower median FWHM ($252\,\mathrm{km\,s^{-1}}$) was reported by Bethermin et al. (2020) for 75 ALPINE-ALMA large programme targets at $4.4 < z < 5.9$, detected in the [CII] 157.7 μm line. These targets have substantially lower SFRs than the strongly lensed galaxies observed by Gullberg et al. (2015) and Nesvadba et al. (2019). A result close to that by Bethermin et al. (2020) was found by Fujimoto et al. (2019) for a sample of 18 galaxies at a higher mean redshift ($5.153 \leq z \leq 7.142$): the weighted average FWHM of the [CII] 157.7 μm line for their sample is $270\,\mathrm{km\,s^{-1}}$.

At still higher redshifts, Tamura et al. (2019) and Hashimoto et al. (2018) reported lower FWHMs of the [OIII] 88.36 μm line for galaxies at $z = 8.31$ ($141 \pm 21\,\mathrm{km\,s^{-1}}$) and at $z = 9.11$ ($154 \pm 39\,\mathrm{km\,s^{-1}}$), respectively. An even lower line width ($\simeq 43\,\mathrm{km\,s^{-1}}$) was derived by Laporte et al. (2017) for a galaxy at $z = 8.38$.

Thus, for ultraluminous submm galaxies the signal dilution due to the modest spectral resolution of the instrument is moderate, up to $z \simeq 5$–6, while it is stronger at higher z and at lower luminosities.

The information on the velocity dispersion of galaxies in high-z proto-cluster cores of submm galaxies is still very limited. Hill et al. (2020) estimated a line-of-sight velocity dispersion $\sigma_r = 376 \pm 68\,\mathrm{km\,s^{-1}}$ for the $z = 4.3$ proto-cluster core discovered by Miller et al. (2018). Oteo et al. (2018) found a substantially higher σ_r ($794 \pm 68\,\mathrm{km\,s^{-1}}$) for their $z = 4.0$ proto-cluster core. However, they argued that the detected galaxies actually belong to two groups, each with a much lower σ_r. Venemans et al. (2007) measured velocity dispersions of forming clusters of galaxies near powerful radio galaxies at $2.0 < z < 5.2$. They found that σ_r increases from $\sim 300\,\mathrm{km\,s^{-1}}$ at $z > 4$ to 500–700 $\mathrm{km\,s^{-1}}$ at $z \sim 3$. In the two lowest redshift fields ($z = 2.86$ and 2.16), the velocity distribution is bimodal, indicating the presence of subgroups with $\sigma_r = 200$–$500\,\mathrm{km\,s^{-1}}$. This shows that, on the one side, the lines from the spatially unresolved cluster cores are spectrally unresolved except at the lowest redshifts and, on the other hand, that the signal dilution is expected to be from moderate to low.

The results for the brightest lines are shown in the right-hand panel of Figure 1. The best lines are [CI] 170.42 μm for $z \lesssim 0.5$, [NII] 205.18 μm for $0.5 \lesssim z \lesssim 0.9$, [CII] 157.7 μm for $0.9 \lesssim z \lesssim 3.4$, [OIII] 88.36 μm for $3.4 \lesssim z \lesssim 4.8$, and [OIII] 51.81 μm for $z \gtrsim 4.8$.

The right-hand panel of Figure 1 shows that the detection limits for [CII] 157.7 μm, [OIII] 88.36 μm, [OI] 63.18 μm, and [OIII] 51.81 μm correspond to values of SFR that are quite close to each other. Hence a substantial fraction of galaxies will be detected both in the [CII] 157.7 μm and [OIII] 88.36 μm lines for $z \gtrsim 2.4$ (when the second line shows up at $\nu < 1000$ GHz). The

https://doi.org/10.1017/pasa.2020.16 Published online by Cambridge University Press

Table 1. Sensitivity in temperature, ΔT (in units of temperature times square root of solid angle), point source detection limits, S_{lim}, and line-detection limits, log (F_{lim}), at selected frequencies, ν, (or wavelengths λ) for a 2-yr survey of 90% of the sky with the instrument described in the text. Both S_{lim} and F_{lim} are at the 5σ significance level. The angular resolution of the instrument, measured by the FWHM (full width at half maximum of the beam) at each frequency, is at the diffraction limit.

ν	λ	FWHM	ΔT	S_{lim}	log (F_{lim})
(GHz)	(mm)	(arcmin)	(μK·arcmin)	(mJy)	(W m^{-2})
100	2.998	3.80	58.70	30.87	−18.988
120	2.498	3.17	51.86	32.73	−18.883
140	2.141	2.72	45.76	33.69	−18.803
160	1.874	2.38	40.38	33.98	−18.742
180	1.666	2.11	35.51	33.61	−18.695
200	1.499	1.90	31.18	32.80	−18.660
220	1.363	1.73	27.33	31.62	−18.635
240	1.249	1.58	23.91	30.18	−18.617
260	1.153	1.46	20.88	28.55	−18.607
280	1.071	1.36	18.23	26.84	−18.601
300	0.999	1.27	15.89	25.07	−18.601
320	0.937	1.19	13.81	23.24	−18.606
340	0.882	1.12	12.02	21.49	−18.613
360	0.833	1.06	10.47	19.82	−18.624
380	0.789	1.00	9.10	18.18	−18.638
400	0.749	0.95	7.94	16.71	−18.652
420	0.714	0.91	6.91	15.27	−18.670
440	0.681	0.86	6.05	14.01	−18.687
460	0.652	0.83	5.30	12.81	−18.707
480	0.625	0.79	4.67	11.78	−18.725
500	0.600	0.76	4.11	10.82	−18.744
520	0.577	0.73	3.66	10.00	−18.761
540	0.555	0.70	3.26	9.27	−18.778
560	0.535	0.68	2.93	8.63	−18.793
580	0.517	0.66	2.65	8.09	−18.806
600	0.500	0.63	2.42	7.64	−18.816
620	0.484	0.61	2.22	7.24	−18.825
640	0.468	0.59	2.06	6.92	−18.831
660	0.454	0.58	1.92	6.67	−18.833
680	0.441	0.56	1.80	6.43	−18.836
700	0.428	0.54	1.70	6.25	−18.836
720	0.416	0.53	1.62	6.12	−18.833
740	0.405	0.51	1.54	6.00	−18.830
760	0.394	0.50	1.47	5.88	−18.827
780	0.384	0.49	1.42	5.83	−18.819
800	0.375	0.48	1.37	5.77	−18.813
820	0.366	0.46	1.33	5.72	−18.806
840	0.357	0.45	1.29	5.68	−18.798
860	0.349	0.44	1.25	5.66	−18.790
880	0.341	0.43	1.22	5.65	−18.781
900	0.333	0.42	1.19	5.63	−18.772
920	0.326	0.41	1.16	5.63	−18.763
940	0.319	0.40	1.14	5.62	−18.754
960	0.312	0.40	1.11	5.63	−18.744
980	0.306	0.39	1.09	5.63	−18.735
1 000	0.300	0.38	1.07	5.64	−18.726

https://doi.org/10.1017/pasa.2020.16 Published online by Cambridge University Press

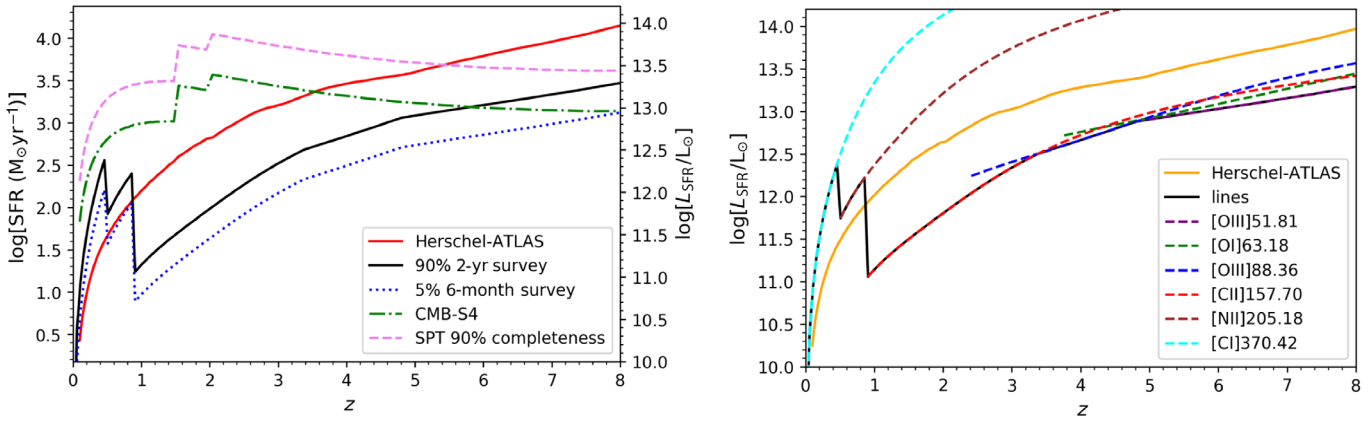

Figure 1. *Left*: Minimum SFR as a function of redshift, for galaxies detected in lines in the 100–1 000 GHz range in an 'all-sky' survey (2 yr, 90% of the sky, solid black line) and for a deep survey 6-month duration over 5% of the sky (dotted blue line); see text for details. The scale on the right refers to the bolometric luminosity due to star formation, L_{SFR}, based on the calibration by Kennicutt & Evans (2012). The solid red line, the green dot-dashed line, and the magenta dashed line show, for comparison, the IR (8–1 000 μm) luminosity, L_{IR}, corresponding to the 4σ detection limits (approximately 90% completeness) of the H-ATLAS survey covering 660 deg^2, to confusion limit of the CMB-S4 survey at 220 GHz expected to cover 43% of the sky (5 mJy; Abazajian et al. 2019), and to the 90% completeness limit (15 mJy) of the South Pole Telescope (SPT; Mocanu et al. 2013) survey covering 2, 500 deg^2, respectively. Here L_{IR} is a measure of the dust-obscured SFR. *Right*: Minimum L_{SFR} (or SFR) corresponding to the 5σ detection limits of the brightest IR/submm lines over the 100–1 000 GHz range, for the 'all-sky' survey.

[OI] 63.18 μm and [OIII] 51.81 μm lines come in at $z \geq 3.7$ and $z \geq 4.8$, respectively.

For comparison, the solid red line in the left-hand panel of Figure 1 also shows the minimum $L_{\rm IR}$, or the minimum dust-enshrouded SFR, among those corresponding to the 4σ detection limits of the H-ATLAS survey (the largest extragalactic survey with *Herschel*, having sensitivities of 29.4, 37.4, and 40.6 mJy at 250, 350, and 500 μm, respectively; Valiante et al. 2016). The monochromatic luminosities corresponding to these detection limits have been converted to $L_{\rm IR}$ using the spectral energy distributions (SEDs) adopted by Cai et al. (2013). More precisely, for $z < 1.5$ we have used the 'warm' (starburst) SED and at $z > 2$ the 'proto-spheroidal' SED; at intermediate redshifts, we considered both SEDs and chose the more favourable one, i.e., the one yielding the lower $L_{\rm IR}$. Since the submm continuum measures only the light re-emitted by dust, while the fine-structure lines measure the total SFR, the comparison of the two measurements, both made by the proposed instrument, provides information on the effective optical depths of galaxies.

3. SFR functions and redshift distributions

To investigate quantitatively the discovery potential of the proposed spectroscopic survey, the relationships between line luminosity and SFR need to be coupled with a model for the redshift-dependent SFR function. We adopted the physically grounded model by Cai et al. (2013). This model is built on the consideration that, in the local Universe, spheroids (i.e., ellipticals and bulges of disc galaxies) are mostly inhabited by old stellar populations (formation redshifts $z \gtrsim 1$–1.5), while the populations of disc galaxies are generally younger, with luminosity-weighted ages mostly $\lesssim 7$ Gyr (cf., e.g., Bernardi et al. 2010), corresponding to formation redshifts $z \lesssim 1$. Thus, spheroid progenitors (referred to as proto-spheroids or proto-spheroidal galaxies) are the dominant star-forming population at $z \gtrsim 1.5$, whereas most of the star formation at $z \lesssim 1.5$ occurs in discs.

These different evolutionary histories are dealt with adopting a 'hybrid' approach. The model provides a physically grounded description of the redshift-dependent co-evolution of the SFR of proto-spheroidal galaxies and of the active nuclei at their centres, while the description of the evolution of late-type galaxies and of AGN associated with them is phenomenological and parametric.

The calculation of the evolving SFR function of proto-spheroids hinges upon the halo formation rate as a function of redshift, z, and of halo mass, $M_{\rm H}$, provided by large-scale N-body simulations. The analytical approximation of the halo mass function, $N(M_{\rm H}, z)$, derived by Sheth & Tormen (1999) was used. The positive term of its time derivative was adopted as a good approximation of the halo formation rate. High resolution N-body simulations (e.g., Wang et al. 2011) showed that, after a fast collapse phase, including major mergers, the halo growth (mostly by minor mergers and diffuse accretion) mainly affects the halo outskirts and has little impact on the inner potential well where the visible galaxy resides. Based on these results, the model assumes that the main drivers of star formation and AGN growth are *in situ* processes. The star-formation history of proto-spheroids is computed by solving a set of equations describing the evolution of gas phases and of the active nucleus, including cooling, condensation into stars, radiation drag, accretion, and feedback from supernovae and from the AGN.

Solving these equations, we obtain the SFR of each galaxy and the bolometric luminosity of the AGN as a function of halo mass, formation redshift, and galactic age. Coupling the SFR($M_{\rm H}, z$) with the halo formation rate we get the SFR function of proto-spheroids at any redshift. As for late-type galaxies, Cai et al. (2013) adopted a phenomenological evolutionary model, with different parameters for starburst and 'normal' disc galaxies. The global (proto-spheroids plus late-type galaxies) SFR functions yielded by the model are in excellent agreement with observational determinations obtained combining information from far-IR/submm, UV, and Lyα surveys (Cai et al. 2014; Mancuso et al.

https://doi.org/10.1017/pasa.2020.16 Published online by Cambridge University Press

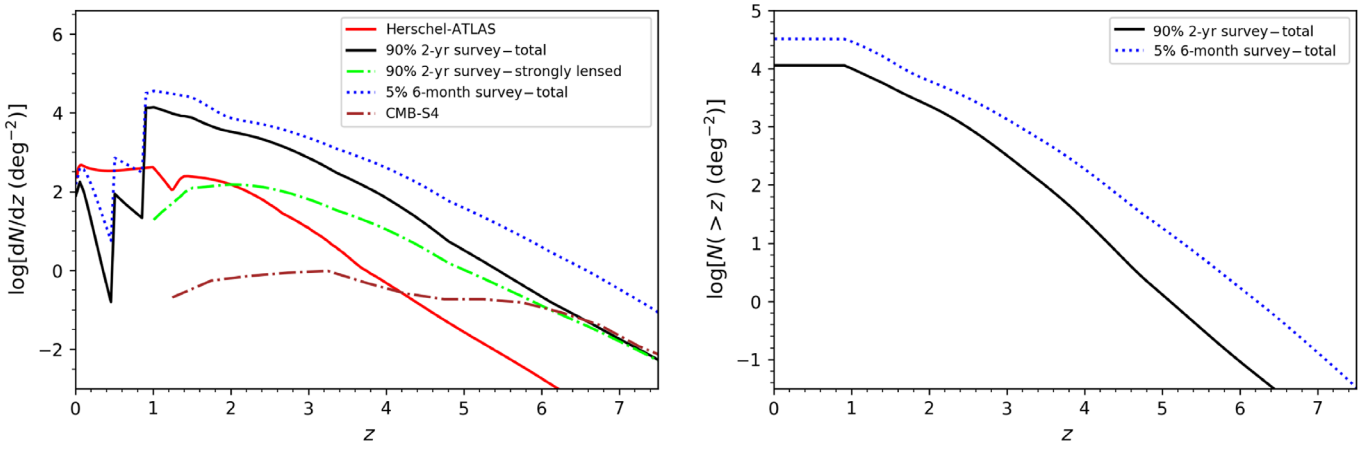

Figure 2. *Left*: Predicted differential redshift distributions of galaxies detected in at least one line by the 'all-sky' survey (2 yr, 90% of the sky, with the solid black line being the total and the dot-dashed green line being for strongly lensed galaxies) and by the 'deep' survey (6 months, 5% of the sky, with the dotted blue line showing the total distribution). For comparison, the solid red line shows the estimated redshift distribution of galaxies detected by the H-ATLAS survey over 660 deg^2 above the 4σ limit in at least one SPIRE channel, based on the Cai et al. (2013) model. The dot-dashed brown line shows the predicted redshift distribution at the confusion limit of the CMB-S4 survey (with an expected sky coverage of 43%), derived from the cumulative distribution in Figure 26 of the CMB-S4 Science Case paper (Abazajian et al. 2019). *Right*: Total cumulative redshift distributions for the 'all-sky' and for the 'deep' survey (solid black line and dotted blue lines, respectively).

2015). Therefore, the results based on them are essentially model independent.

Figures 2 and 3 show that the spectroscopic survey will allow us to extend the study of the global star-formation history and the build-up of metals and dust all the way through the epoch of reionisation. The survey will detect thousands of star-forming galaxies at $z \simeq 6$ and several tens at $z \simeq 8$. Note that the predicted abundances of high-z galaxies reported in these figures may be underestimated if the stellar IMF becomes more top-heavy (i.e., has a larger fraction of massive stars compared to standard IMFs) at high-z, as suggested by theoretical arguments (e.g., Papadopoulos et al. 2011) and indicated by some observational evidence (Zhang et al. 2018b). A more top-heavy IMF would yield higher surface densities of ultra-luminous high-z galaxies. An excess of $z \gtrsim 4$ dusty galaxies over model expectations has been reported, but the issue is controversial (see Cai et al. 2020, for a recent discussion and references).

The excellent sensitivity of the instrument, the high luminosity of the [CII] 157.7 μm, [OIII] 88.36 μm, [OI] 63.18 μm, and [OIII] 51.81 μm lines, and the immunity to the confusion limit make the spectroscopic survey far more efficient than broadband surveys at detecting high-z star-forming galaxies. This is illustrated by the comparison with the estimated redshift distribution of H-ATLAS galaxies.

The redshift distribution of the spectroscopic survey (Figure 2) peaks at $z \simeq 1$–1.5. The brightest line within the frequency range covered by the instrument varies with redshift (see the right-hand panel of Figure 1). These variations produce the indentations at low z and the secondary peak at $z \simeq 0.6$. The solid red line shows, for comparison, the estimated redshift distribution of galaxies detected by the H-ATLAS survey above the 4σ limit in at least one SPIRE channel (based on the Cai et al. 2013 model). The dip at $z \simeq 1.5$ corresponds to the change of the dominant star-forming population: late-type plus starburst galaxies and proto-spheroidal galaxies at lower and higher redshifts, respectively.

4. Strongly lensed galaxies

Figures 2 and 3 also show that most spectroscopically detected $z \gtrsim 4$ galaxies and the brightest galaxies at lower redshifts are strongly lensed (see discussions in Perrotta et al. 2002; Negrello et al. 2007; Paciga, Scott, & Chapin 2009; Lima et al. 2010). The availability of large samples of strongly lensed galaxies out to high redshifts will drive a real breakthrough in the study of the early evolutionary phases of galaxies. The *Herschel* surveys H-ATLAS and HerMES, the *Planck* all-sky survey, and the SPT survey have already provided several hundreds of lensed galaxy candidates, with painstaking follow-up campaigns worldwide and at all wavelengths (e.g., Negrello et al. 2010, 2014, 2017a; Lupu et al. 2012; Vieira et al. 2013; Wardlow et al. 2013; Hezaveh et al. 2013; Cañameras et al. 2015; Harrington et al. 2016; Nayyeri et al. 2016; Díaz-Sanchez et al. 2017; Yang et al. 2017; Bakx et al. 2018; Harrington et al. 2018; Massardi et al. 2018; Dannerbauer et al. 2019b).

Strong lensing not only boosts the observed global flux by a factor μ but also increases the angular sizes of galaxies by an average factor of $\mu^{1/2}$. Since the magnification μ can be several tens, the expansion of the image can be quite substantial. The study in great detail of the internal structure and kinematics of galaxies will then become accessible to high resolution instruments like ALMA or the *James Webb Space Telescope* (*JWST*).

A spectacular demonstration of the power of strong gravitational lensing in this respect was provided by ALMA 0.1 arcsec resolution observations of the *Planck* source PLCK G244.8+54.9 at $z \simeq 3.0$, with $\mu \simeq 30$ (Cañameras et al. 2017). These observations reached the astounding spatial resolution of 60 pc, comparable to the size of GMCs (around 40–100 pc). Very recently, ALMA high resolution observations of a strongly lensed, normal star-forming galaxy at $z = 1.06$ (the 'Cosmic Snake') even reached a spatial resolution of 30 pc in the source plane (Dessauges-Zavadsky et al. 2019). Intriguingly, the 17 identified GMCs in this source have different physical properties on average than those of nearby galaxies.

https://doi.org/10.1017/pasa.2020.16 Published online by Cambridge University Press

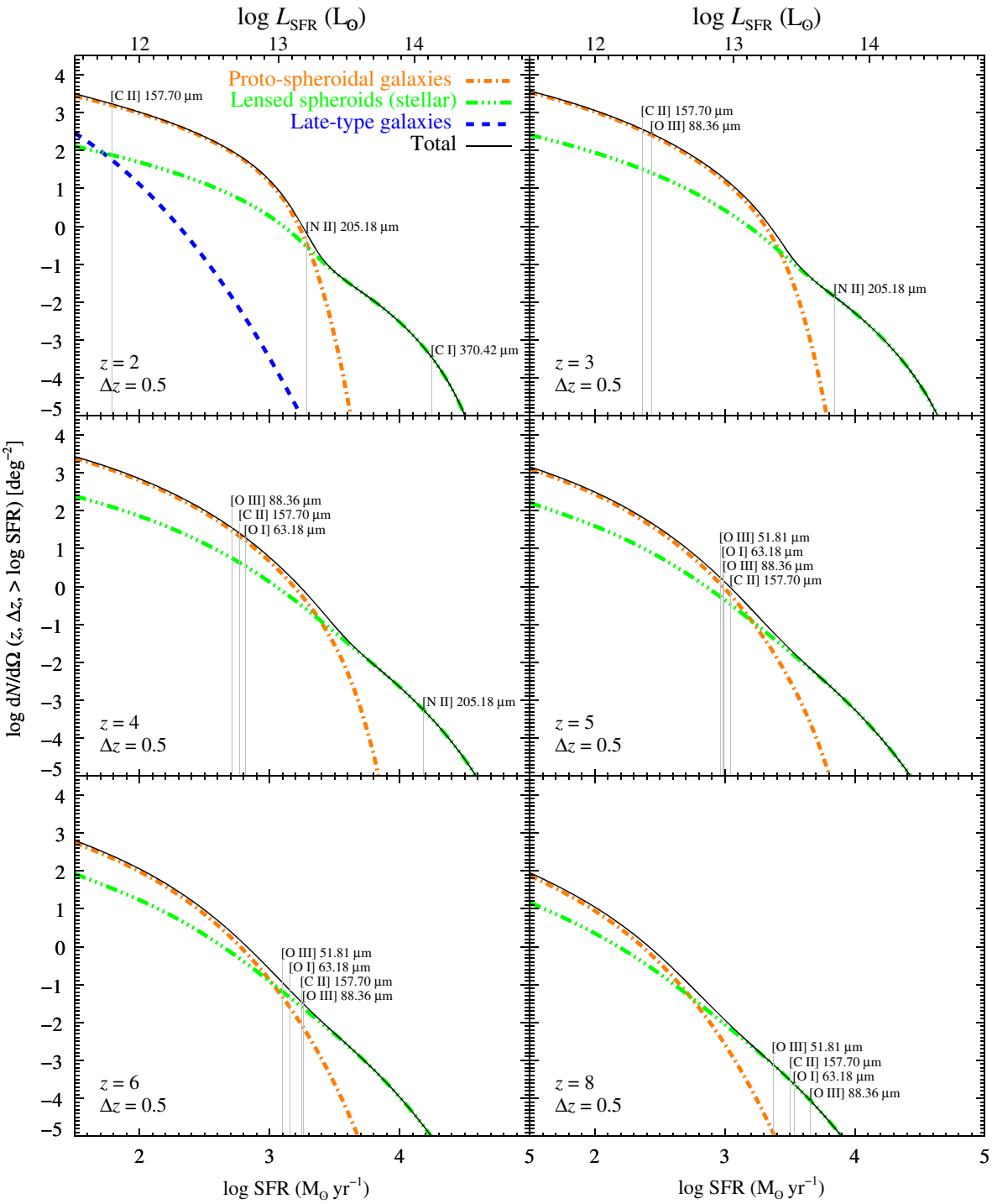

Figure 3. Cumulative SFR functions of galaxies within $\delta z = 0.5$ derived from the Cai et al. (2013) model at redshifts from 2 to 8. The vertical lines show the SFRs corresponding to the 5σ line-detection limits of the brightest lines.

AGN-driven outflows are a key ingredient of current galaxy evolution models (see, e.g., Heckman & Best 2014), since they provide the most plausible explanation for the deviation of the galaxy stellar mass function from the halo mass function at large masses, i.e., for the low star-formation efficiency in massive halos, only less than 10 % of baryons initially present in such halos are used to form stars. However, information on the effect of feedback on the direct fuel for star formation (namely, molecular gas) during the epoch of the most active cosmic star formation is largely missing, due to the weakness of spectral signatures of molecular outflows.

Gravitational lensing allows us to overcome these difficulties. Cañameras et al. (2017) obtained CO spectroscopy with a velocity resolution of 40–50 km s^{-1}. This spectral resolution makes possible a direct investigation of massive outflows driven by AGN

https://doi.org/10.1017/pasa.2020.16 Published online by Cambridge University Press

feedback at high z, with predicted velocities of order 1000 km s^{-1} (King & Pounds 2015). Spilker et al. (2018) and Jones et al. (2019) detected, by means of ALMA spectroscopy, massive molecular outflows in two strongly lensed galaxies at $z = 5.3$ and $z = 5.7$, respectively, discovered by SPT survey. Cañameras et al. (2018) detected a molecular wind signature in the strongly lensed galaxy PLCK G165.7+49.0, discovered by *Planck*, at $z = 2.2$, with magnification factors between 20 and 50 over most of the source of emission.

5. Unlensed galaxy populations

The evolution of the dust-obscured star formation is still poorly known. Gruppioni et al. (2013), Magnelli et al. (2013), and Wang et al. (2019b) estimated the IR luminosity functions of galaxies based on the *Herschel* PACS and SPIRE survey data. Above $z \simeq 2.5$, the overwhelming majority of redshifts are photometric (at $z > 3$, there are only about 4–6 % spectroscopic redshifts, depending on the survey field). Substantially increasing the fraction of spectroscopic redshifts is hard because of the faintness of these galaxies in the optical/near-IR.

All these studies required the use of optical/near-IR data for photometric redshift estimates. This means that heavily dust-obscured galaxies are missed. Recent investigations (Wang et al. 2019a; Dudzevičiūtė et al. 2019; Williams et al. 2019) have shown that a substantial fraction of massive galaxies at $z > 3$ are optically dark.

The proposed spectroscopic survey will provide an unbiased determination of the redshift-dependent IR luminosity function up to $z \simeq 6$. For the first time, we will have spectroscopic redshifts for a huge number of lensed and non-lensed DSFGs, obtained in an unbiased way, independent of the identification/pre-selection method. Out to $z \simeq 4$, the luminosity functions will be determined down to below the characteristic $L_{\star,\rm IR}$. At $z \gtrsim 2.4$, we expect detections in both the [CII] 157.7 μm and the [OIII] 88.36 μm line.

Such an all-sky survey offers the opportunity to search for non-lensed, hyper-luminous infrared galaxies (HyLIRGs; $L_{\rm IR} > 10^{13} L_{\odot}$). Currently, only a few examples are known in the distant Universe (Fu et al. 2012; Ivison et al. 2013; Riechers et al. 2013), whilst models predict a factor of 2 higher numbers of HyLIRGs (Cai et al. 2013). Furthermore, the fraction of HyLIRGs within the brightest *Herschel* galaxies is still unknown.

We note that, in particular, far-IR fine-structure lines seem to be the best way to obtain spectroscopic redshifts of rest-frame UV-selected galaxies beyond $z = 7$ (e.g., Inoue et al. 2016; Carniani et al. 2017; Laporte et al. 2017; Hashimoto et al. 2018; Smit et al. 2018; Tamura et al. 2019).

6. Comparison and synergies with other large-area surveys

Large samples of strongly lensed and unlensed dusty galaxies are expected to also be obtained by next generation CMB experiments, like the 'CMB-S4' (ground-based; Abazajian et al. 2019) and the space-borne Probe of Inflation and Cosmic Origins (*PICO*; Hanany et al. 2019). However, the depth of *PICO* surveys is limited by confusion, due to the modest telescope size (1.4 m).

Confusion is a limiting factor also in the case of the 6-m telescopes used as part of CMB-S4, since they operate at mm wavelengths. Another practical limit is set by atmospheric noise. If the effective depths of the CMB-S4 surveys are similar to those of the SPT (a 10-m telescope), the detection of only a few hundred strongly lensed galaxies at $z \geq 6$ is expected. However the CMB-S4 survey will provide deeper photometry at mm wavelengths, which is important to quantify the cold dust emission.

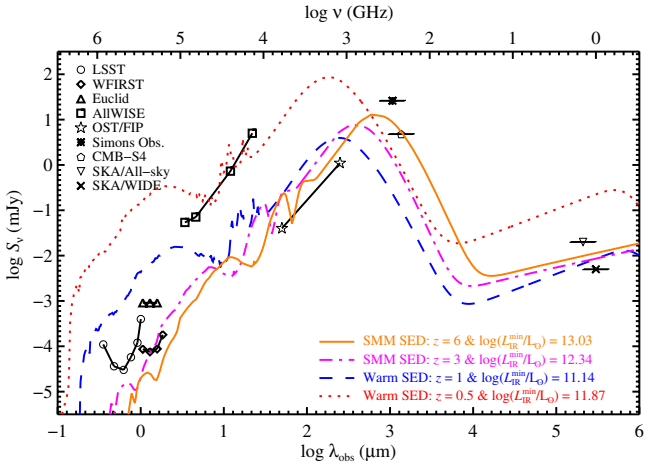

Figure 4. Detection limits (5σ) of large area surveys at optical (LSST Science Collaboration 2009), near-IR (*Euclid* and *WFIRST*, Laureijs et al. 2011; Spergel et al. 2015), mid-IR (AllWISE, Cutri et al. 2013, and http://wise2.ipac.caltech.edu/docs/release/allwise/expsup/sec2_3a.html), far-IR/submm (OST/FIP, CMB-S4, and Simons Observatory, Abazajian et al. 2019; Ade et al. 2019; Meixner et al. 2019), and radio (SKA, Prandoni & Seymour 2015) wavelengths compared with model SEDs of galaxies having the minimum L_{IR} detectable in lines at $z = 0.5$, 1, 3, and 6. At the two lower redshifts, we have adopted the 'warm' (starburst) SED, while at the two higher redshifts, we use the proto-spheroid SED (Cai et al. 2013).

A great advantage of a spectroscopic survey is the direct measurement of redshifts, while surveys of the continuum require a lengthy follow-up programme that may be impractical for hundreds of thousands of optically very faint or almost invisible (e.g., Dannerbauer et al. 2002; Younger et al. 2007; Dannerbauer et al. 2008; Wang et al. 2019a) galaxies. In addition, the target lines allow us to single out the star-formation luminosity. It may be difficult to disentangle this from the AGN contribution using broadband photometry alone (Symeonidis et al. 2016; Symeonidis 2017).

As illustrated in Figure 4, there are important synergies with large-area surveys at other wavelengths. For example, the Large Synoptic Survey Telescope (LSST; LSST Science Collaboration 2009) will survey 20 000 deg^2 of the sky in six photometric bands. The final coadded depths (point sources; 5σ) are $u = 26.3$, $g = 27.5$, $r = 27.7$, $i = 27.0$, $z = 26.2$, and $y = 24.9$ AB magnitudes.

Euclid (Laureijs et al. 2011) will cover 15 000 deg^2 of the sky to Y, J, and $H = 24$ mag. The *Wide Field Infrared Survey Telescope* (*WFIRST*; Spergel et al. 2015) will carry out large area, deep multi-filter imaging surveys at high galactic latitudes. As an example, we show in Figure 4 the expected depths for a nominal 2.5-yr survey of 2 500 deg^2 down to $J \sim 27$ AB mag. The AllWISE survey (Wright et al. 2010) has already provided shallower all-sky surveys at 3.4, 4.6, 12, and 22 μm.

The Far-infrared Imager and Polarimeter (FIP) on the *Origins Space Telescope* (OST; Meixner et al. 2019) will deliver an ultra-wide-field survey (10 000 deg^2) at 250 μm down to the confusion limit (1.1 mJy) and a wide survey (500 deg^2) at 50 μm down to 40 μJy. The Simons Observatory (Ade et al. 2019) Large Aperture Telescope will survey 40% of the sky with arcmin resolution down to 26 mJy at 280 GHz. CMB-S4 (Abazajian et al. 2019) will reach the confusion limit (4.8 mJy at 220 GHz) over a large fraction of the sky, and will cover several frequency bands.

https://doi.org/10.1017/pasa.2020.16 Published online by Cambridge University Press

The Square Kilometre Array (SKA) 'all-sky' survey will cover 31 000 deg^2 at 1.4 GHz down to 20 μJy beam^{-1} (5σ), while the SKA/Wide survey at around 1 GHz will reach 5 μJy beam^{-1} (5σ) over 1 000 deg^2 (Prandoni & Seymour 2015).

As illustrated in Figure 4, the *WFIRST*, the *Origins*/FIP and the SKA/Wide surveys are expected to detect practically all the dusty galaxies seen in lines in our proposed spectroscopic survey, although over limited sky areas. On the other hand, the other surveys mentioned above will also detect a substantial fraction of them, thus providing complementary information on stellar and dust components.

7. Revealing galaxy proto-clusters via dusty starbursts

N-body simulations in the framework of the currently standard ΛCDM cosmology have elucidated how primordial perturbations have grown into collapsed halos distributed within a filamentary structure (the cosmic web, e.g. Springel et al. 2005; Boylan-Kolchin et al. 2009). However an observational validation of how these objects are assembled is still missing. Understanding the full evolutionary history of present-day galaxy clusters is of fundamental importance for the observational validation of the formation history of the most massive dark-matter halos, a crucial test of models for structure formation, as well as for investigating the impact of environment on the formation and evolution of galaxies (Kravtsov & Borgani 2012; Overzier & Kashikawa 2019; Dannerbauer et al. 2019a).

To address the many still open questions on cluster formation and evolution, we need to follow all their evolutionary stages through cosmic time, starting from their progenitors, galaxy-clusters-in-formation, so-called 'proto-clusters' (for a review, see Overzier 2016). This needs a coordinated multi-frequency effort. Cluster identification via classical methods (optical/IR imaging and detection of X-ray or SZ signals from the hot IntraCluster Medium (ICM)) has been very effective at relatively low redshifts. Samples of SZ-selected clusters have been recently extended to a few thousand objects, primarily thanks to surveys with the *Planck* satellite (Planck Collaboration XXVII 2016), the SPT (Bleem et al. 2020), and the Atacama Cosmology Telescope (ACT; Hilton et al. 2018). A few thousand clusters have also been detected in X-rays (Klein et al. 2019). Both ICM-based techniques have yielded just a handful of clusters above $z \simeq 1.5$. The *e-ROSITA* all-sky survey is expected to boost the number of X-ray-detected clusters to around 10^5, but again few detections are expected at $z \gtrsim 1.5$ (Grandis et al. 2019). There is also a limit to detecting X-rays and the SZ effect at very high redshifts because of the lack of virialised gas.

Galaxy cluster searches looking for overdensities of galaxies in large-area optical/IR surveys (e.g., Oguri et al. 2018; Wen & Han 2018; Gonzalez et al. 2019) are generally limited to $z \lesssim 1.5$ due to the subtle density contrasts of the object. Observations indicate that $z \simeq 1.5$ corresponds to a critical epoch in galaxy cluster evolution. At lower redshifts, the global SFR of galaxies is anti-correlated with local density (Dressler 1980; Kauffmann et al. 2004; Lemaux et al. 2019). However, the specific SFR (i.e., the SFR per unit stellar mass) increases faster in clusters than in the field, catching up with that in the field at $z \simeq 1.5$ (Alberts et al. 2014, 2016; Wagner et al. 2017). Thus, galaxy clusters selected through optical/IR observations are rare at $z \gtrsim 1.5$ (Gobat et al. 2011).

Above $z \simeq 1.5$, when a large fraction of member galaxies are in the dust-obscured star-formation phase (e.g., Dannerbauer et al. 2014; Clements et al. 2016; Kato et al. 2016; Wagner et al. 2017; Nantais et al. 2017), proto-cluster searches are most conveniently carried out at submm wavelengths. Negrello et al. (2005) predicted the detection by *Planck* and *Herschel* submm surveys of unresolved intensity peaks made by the summed emission of dusty star-forming high-z proto-cluster members within the beam. Motivated by this work, Planck Collaboration Int. XXXIX (2016) have reported the detection of 2 151 proto-cluster candidates over the cleanest 26% of the sky—these are unresolved sources with 'red' submm colours, consistent with redshifts $z > 2$.

Follow-up observations of a subset of these sources with *Herschel* (Planck Collaboration Int. XXVII 2015) have shown that, apart from a tiny fraction of strongly lensed galaxies (the GEMS sample, see Cañameras et al. 2015), they are associated with overdensities of DSFGs. However, Negrello et al. (2017b) argued that most of them are probably not individual proto-clusters, but could be made of physically unrelated high-z structures falling by chance within the relatively large *Planck* beam (FWHM $\simeq 5$ arcmin). This has been confirmed by spectroscopic measurements and/or photometric redshift estimates for two objects, showing that each consists of two independent overdensities along the line of sight (Flores-Cacho et al. 2016; Kneissl et al. 2019).

The confusion problem (blending of independent proto-clusters along the line of sight) affecting *Planck* surveys is due to its poor angular resolution. The instrument considered here has angular resolution ≤1 arcmin at $\nu \geq 380$ GHz (cf. Table 1). This is the ideal angular resolution for searches of submm-bright proto-clusters. The angular correlation function of faint submm galaxies measured by Chen et al. (2016) in photometric redshift bins up to $z \simeq 5$ showed that the 1-halo component, corresponding to the source distribution within the proto-cluster halo, dominates at $\theta \lesssim 1$ arcmin. This is in keeping with the results of Alberts et al. (2014) on 274 clusters with $0.3 \leq z \leq 1.5$. They found that the density of IR-emitting cluster members clearly exceeds that of the background field level only within 0.5 Mpc of the cluster centre. Such a linear scale corresponds to an angular scale of about 1 arcmin at redshifts in the range 1.5–2.5.

The clustering measurements by Chen et al. (2016) also gave clear indications of a steepening of the correlation function on arcsec angular scales. Negrello et al. (2017b) modelled this in terms of an additional component with a spatial correlation function $\xi(r) \propto r^{-3.3}$. This component, which dominates for $r \lesssim 50$ kpc, may represent the cluster core. Submm-bright proto-cluster cores, with linear diameters of order 100 kpc, have been discovered by Ivison et al. (2013, 2019) at $z = 2.41$, Gómez-Guijarro et al. (2019) at $z = 2.2$ and $z = 2.6$, Wang et al. (2016) at $z = 2.5$, and Miller et al. (2018) at $z = 4.3$. Oteo et al. (2018) reported the identification of a dusty proto-cluster core at $z = 4.0$, whose member galaxies are distributed over a 260 kpc × 310 kpc region. Additionally Lacaille et al. (2019) spectroscopically confirmed the detection of two submm proto-clusters at $z \simeq 2.8$ and $\simeq 2.3$, with 1 arcmin angular radius.

The spectroscopically confirmed proto-cluster *cores* listed above are unresolved at the resolution of the instrument, except perhaps at the highest frequencies, where the maps can be degraded to arcmin resolution. The summed IR luminosities of detected members of the spectroscopically confirmed high-z proto-clusters (lower limits to the proto-cluster total IR luminosities) range from a few to several × 10^{13} $L_\odot$ and are all well above the line-detection limits (see Figure 5) of our proposed surveys.

High-z proto-clusters with enhanced star formation on larger (few to several Mpc) scales have also been reported by

https://doi.org/10.1017/pasa.2020.16 Published online by Cambridge University Press

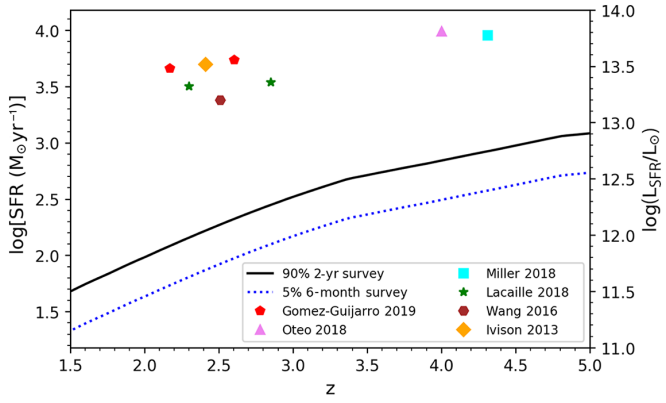

Figure 5. SFRs of the spectroscopically confirmed, submm-bright proto-cluster cores discovered so far, compared with the minimum SFRs detectable at 5σ by the 'all-sky' (solid black line; 2 yr, 90% of the sky) and by the 'deep' (dotted blue line; 5% of the sky, six months) spectroscopic surveys. The data points are Ivison et al. (2013) at $z = 2.41$; Gómez-Guijarro et al. (2019) at $z = 2.171$ and $z = 2.602$; Wang et al. (2016) at $z = 2.51$; Miller et al. (2018) at $z = 4.31$; Oteo et al. (2018) at $z = 4.0$; and Lacaille et al. (2019) at $z \simeq 2.85$ and $\simeq 2.30$.

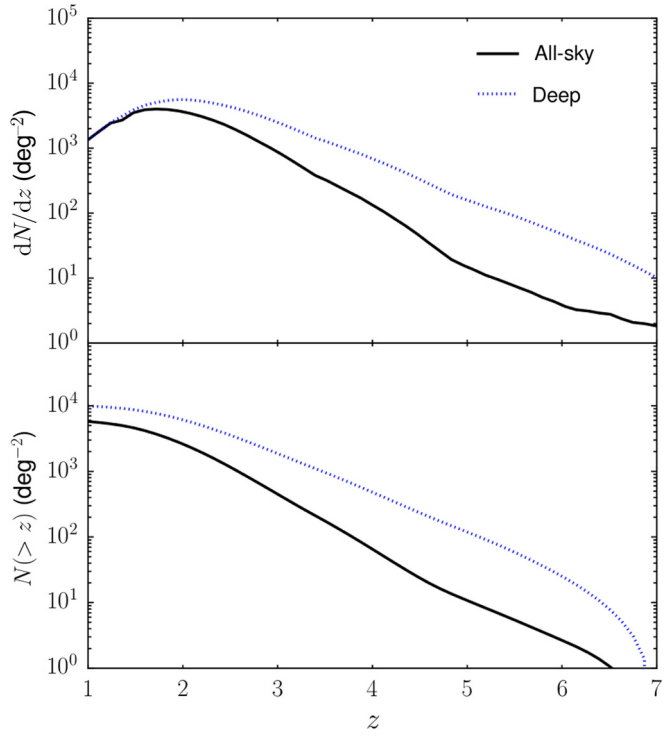

Figure 6. Predicted differential and cumulative redshift distributions (upper and lower panels, respectively) of proto-clusters detected in at least one line by the 'all-sky' survey (2 yr, 90% of the sky; solid black line) and by the deep survey (6 months, 5% of the sky; dotted blue line). We expect the detection of tens of millions of proto-clusters at $z \simeq 2$ and of tens of thousands of them at $z \simeq 6$.

Dannerbauer et al. (2014), Casey et al. (2015), Kato et al. (2016), Hung et al. (2016), and Umehata et al. (2019). *All* proto-clusters with similar properties will be detected by our spectroscopic survey.

As illustrated in Figures 6 and 7, the instrument considered here will detect millions of proto-clusters at the peak of cosmic star-formation activity ($z = 2$–3). For a large fraction of proto-clusters, especially at $z \geq 2.4$, at least two lines will be detected, allowing a solid redshift determination without requiring follow-up observations.

8. Comparison with other large-area cluster surveys

No other foreseen survey can do anything similar to the future spectroscopic satellite. *Euclid*'s 'Wide' survey over 15 000 deg^2 is expected to detect galaxy clusters and proto-clusters only out to $z \simeq 2$. The estimated surface density of clusters detected at 5σ in the redshift range $1.5 \leq z \leq 2$ is $\simeq 0.19$ deg^{-2} (Sartoris et al. 2016, see their Figure 3).

A survey of 8 300 deg^2 by *WFIRST* (Spergel et al. 2015) is expected to detect 20 000 clusters with masses $M_{\rm cl} \geq 7.4 \times 10^{13}$ M$_\odot$ at $z = 1.5$–2 and 2 800 clusters at $z = 2$–2.5 for the same masses. The corresponding surface densities are of 2.4 and 0.34 deg^{-2}, respectively.

For comparison, we expect around 2 000 deg^{-2} (1 300 deg^{-2}) detections in the [CII] 157.7 μm line only and $\simeq 5$ deg^{-2} ($\simeq 0.4$ deg^{-2}) detections in two lines ([CII] 157.7 μm and [NII] 205.18 μm) at $1.5 \leq z \leq 2$ ($2.0 \leq z \leq 2.5$), as shown in Figure 7.

Cluster searches with ground-based, large-area optical surveys like LSST (LSST Science Collaboration 2009) and the Javalambre Physics of the Accelerating Universe Astrophysical Survey (J-PAS; Benitez et al. 2014) are limited to $z < 1.5$. As mentioned above, the X-ray cluster survey of *e-ROSITA* is also limited to $z \lesssim 1.5$ (Grandis et al. 2019).

The most extensive optical search for high-z proto-clusters is being conducted using a wide-field survey with the Hyper Suprime-Cam (HSC) instrument mounted at the prime focus of the Subaru telescope. The wide HSC survey will cover 1 400 deg^2. Toshikawa et al. (2018) carried out a blind search for proto-clusters at $z \simeq 3.8$ over an area of 121 deg^2 using colour criteria to select galaxies at $z \simeq 3.3$–4.2. They found 216 overdensities that were significant at the $> 4\sigma$ level. The estimated comoving density of these objects is 1.4×10^{-7} Mpc^{-3} for the cosmology adopted here. At higher redshifts, Higuchi et al. (2019) reported 14 and 26 proto-cluster candidates at $z = 5.7$ and $z = 6.6$, covering an area of 14 and 16 deg^2, respectively.

Kubo et al. (2019) reported statistical evidence of submm emission from HSC candidate proto-clusters in *Planck* high-frequency maps, confirming the ubiquity of intense star formation in high-z proto-clusters. The estimated average IR luminosity and SFR are well above the detection limits of the proposed spectroscopic survey.

At $z = 3.75$, i.e., close to the redshift of the optical search by Toshikawa et al. (2018), the spectroscopic survey will detect 100 deg^{-2} proto-clusters in the [CII] 157.7 μm line and 50 deg^{-2} also in the [OIII] 88.36 μm line. The corresponding comoving volume densities are 1–2×10^{-5} Mpc^{-3}, i.e., about two orders of magnitude higher than that achieved by Toshikawa et al. (2018). As pointed out by the latter authors, overdensity searches via optical imaging surveys are expected to be highly incomplete (completeness around 6 %) because most overdensities are swamped by projection effects. On the contrary, the statistical detection on *Planck* maps of large SFRs in optically selected proto-clusters suggests a high completeness level for the planned spectroscopic survey.

It is important to stress that the proposed instrument can measure both the SFR and the SZ effect in clusters. It will thus

https://doi.org/10.1017/pasa.2020.16 Published online by Cambridge University Press

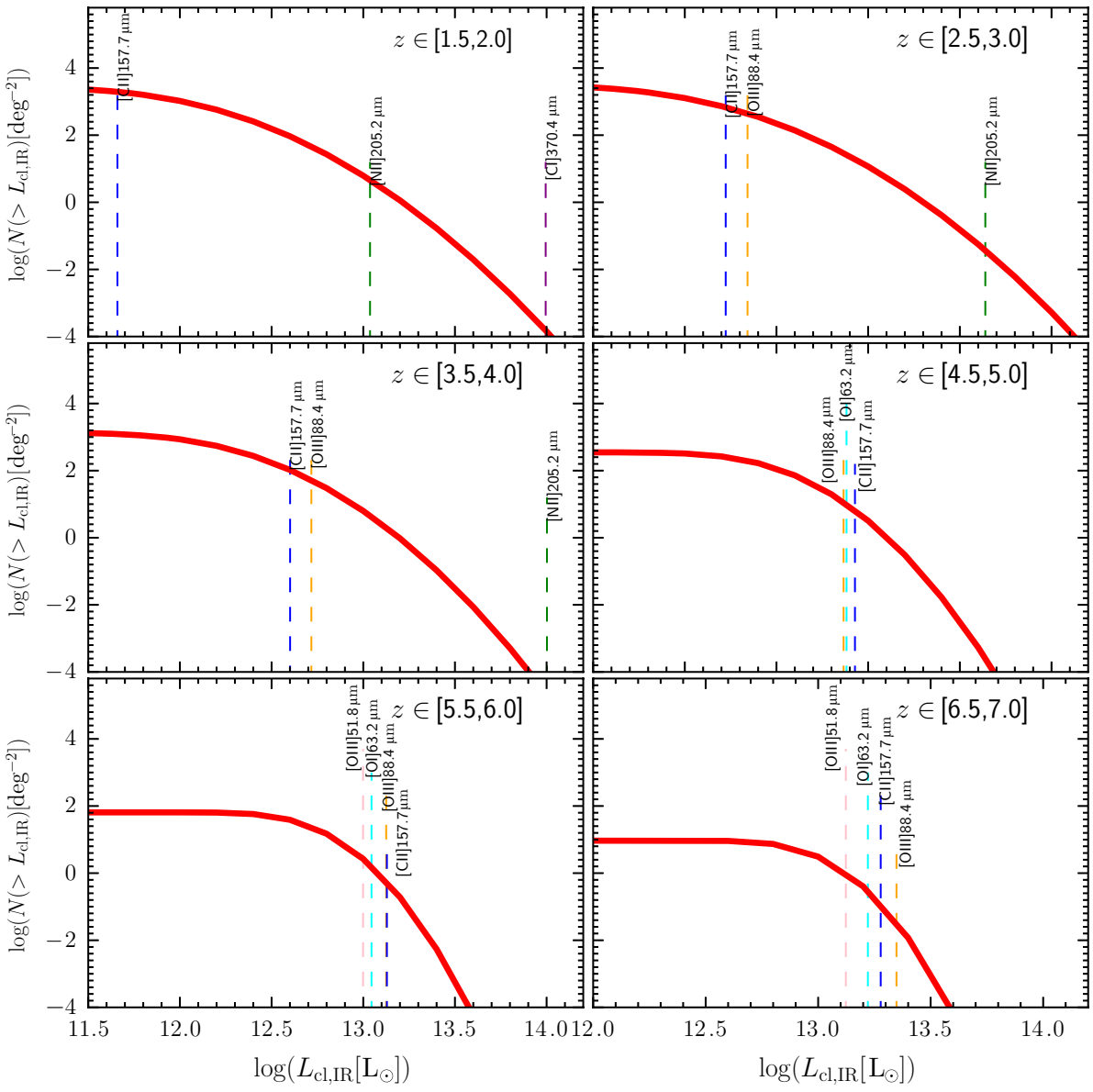

Figure 7. Cumulative IR (8–1 000 μm) luminosity functions of proto-clusters within $\delta z = 0.5$ at six redshifts. The predictions are based on the model of Negrello et al. (2017b). The line luminosities corresponding to L_{IR} were computed as described in the text. The vertical lines show the detection limits for the brightest lines, assuming the instrument performances described in the text. Such an instrument will detect strongly lensed galaxies (cf. Figure 3) and proto-clusters of dusty galaxies all the way out to the reionisation redshift.

simultaneously probe the evolution of star formation in dense environment and of the hot IGM, allowing us to investigate the relationship between the two aspects of cluster evolution. It will thereby provide key data on the still unexplored, crucial transition period at $z \simeq 1.5$–2 when cluster galaxies were vigorously forming stars and at the same time the hot IGM was taking root.

Figure 7 shows that the spectroscopic survey will detect enough proto-clusters within relatively narrow redshift bins to accurately measure their two-point spatial correlation, $\xi(r)$, as a function of redshift out to $z \simeq 6$ and, at fixed z, as a function of $L_{\rm IR}$ (or equivalently of SFR). From the function $\xi(r)$, we can infer the effective halo mass (Sheth et al. 2001), so that the observed proto-cluster abundance provides constraints on the evolution of the high-mass tail of the halo mass function and on the relationship between halo mass and $L_{\rm IR}$ or SFR.

Note that the abundance and clustering of galaxy clusters are both probes of large-scale structure growth. Their determination as a function of mass and redshift enables us to constrain cosmological parameters primarily through the linear growth rate of perturbations. This has been proved to be competitive with and complementary to other probes (e.g., Planck Collaboration XXIV 2016; de Haan et al. 2016; Sridhar et al. 2017).

At lower redshifts, the comparison of cluster samples detected via star formation and via the SZ effect will quantify the history of star-formation quenching in galaxy clusters, a still open issue (Boselli et al. 2016; Rodríguez-Muñoz et al. 2019). In particular, we will learn about the quenching timescale at different redshifts and for different cluster halo masses, inferred from the amplitude of the SZ effect, and of the ICM density inferred from X-ray observations, e.g., from *e-ROSITA*. This is key information for

https://doi.org/10.1017/pasa.2020.16 Published online by Cambridge University Press

identifying the mechanism(s) responsible for the environmental quenching.

9. Conclusions

The high-sensitivity spectroscopic and imaging surveys carried out by the space mission proposed by Delabrouille et al. (2019) will revolutionise our view of galaxy evolution and of the growth of galaxy clusters.

Spectroscopy enables full exploitation of the sensitivity of present-day instrumentation, bypassing the confusion limits that severely constrain the depth of submm surveys with telescopes of the 3-m class, like that of the *Herschel* Observatory.

The high luminosity of far-IR lines, such as [CII] 157.7 μm, [OIII] 88.36 μm, [OI]63.18μm, and [OIII] 51.81 μm, makes it possible to detect, at $z > 1$, star-forming galaxies with SFRs about one order of magnitude lower that those reached by the *Herschel*-ATLAS survey. Moreover, we have argued that these fine-structure lines track the full SFR, not only the dust-obscured fraction measured by the far-IR/submm continuum.

Most importantly, the spectroscopic survey directly provides the 3D distribution of star-forming galaxies all the way through the reionisation epoch. Many tens of millions of galaxies will be detected over the redshift range $1 < z < 3$ (Figure 2) where the cosmic SFR peaks. SFRs well below those of typical galaxies at these redshifts will be reached (Figures 1 and 3). For example, at $z = 2$ the [CII] 157.7 μm line will allow the detection of SFRs down to about 60 $M_\odot$ yr^{-1} by the 'all-sky' survey and down to 30 $M_\odot$ yr^{-1} for the 'deep' survey. Our conservative estimates, which do not allow for the possibility of a top-heavier IMF at high z indicated by theoretical arguments and by some observational results (see Cai et al. 2020, for a discussion), yield the detection of thousands of galaxies at $z \simeq 6$ and of several tens at $z \simeq 8$.

This outcome is far better than can be achieved by existing and forthcoming continuum surveys which, moreover, require time-consuming redshift follow-up programmes that are impractical for millions of optically very faint sources.

The spectroscopic survey will detect millions of strongly lensed galaxies, which dominate the bright tails of the high-z SFR functions, above uncorrected SFRs of a few thousand $M_\odot$ yr^{-1}. Additionally, strong lensing will allow us to probe SFR functions below the nominal detection limit.

The brightest strongly lensed galaxies are obvious targets for follow-up observations with high-resolution instruments like ALMA or *JWST*. The combination of their extreme luminosity with the stretching of their images offers a unique possibility of peering into the internal structure of high-z galaxies down to scales of tens of parsecs, comparable to or smaller than the size of giant molecular clouds in the Milky Way. Data at this resolution are the only way to directly investigate the complex physical processes driving the early evolution of galaxies.

The arcmin (or better) angular resolution at submm wavelengths of the proposed survey is ideal to detect proto-cluster cores out to $z \simeq 7$. The summed line emission of star-forming member galaxies within the beam of the instrument makes these objects produce the brightest intensity peaks at each redshift. Proto-clusters can thus be detected independently of whether they contain the hot IGM that would make them detectable in X-rays or via the SZ effect.

We predict the spectroscopic detection of millions of proto-clusters at $z > 1.5$, i.e., in the redshift range hardly accessible to classical cluster-detection methods. This will provide a complete view of the star-formation history in dense environments. The statistical detection of intense star formation in optically selected high-z proto-clusters (Kubo et al. 2019) suggests that the planned spectroscopic survey will have a high completeness level.

Enough proto-clusters will be detected within relatively narrow redshift bins to accurately measure their clustering $\xi(r, z)$ out to $z \simeq 6$ and, at fixed z, as a function of their SFR. Since $\xi(r)$ allows us to estimate the halo mass, we can derive the first observational constraints on the evolution of the high-mass tail of the halo mass function and on the relationship between halo mass and SFR.

At lower redshifts ($z \lesssim 1.5$–2), the mission will simultaneously measure the SFR and the SZ effect for early structures. In combination with X-ray data from *e-Rosita* and with data from optical surveys measuring stellar masses, this will elucidate several key issues, e.g., the transition from the active star-forming to passive evolution phases of cluster members, the origin of the hot IGM, and the mechanisms responsible for the environmental quenching of star formation.

In all these areas, the proposed spectroscopic survey transcends any other foreseen project.

Acknowledgements. We are grateful to the referee for useful comments. H.D. acknowledges financial support from the Spanish Ministry of Science, Innovation, and Universities (MICIU) under the 2014 Ramón y Cajal programme RYC-2014-15686 and AYA2017-84061-P, the latter being co-financed by FEDER (European Regional Development Funds). M.B. acknowledges partial financial support from the Italian Ministero dell'Istruzione, Università e Ricerca, through the grant 'Progetti Premiali 2012—iALMA' (CUP C52I13000140001) and from INAF under PRIN SKA/CTA FORECaST. Z.Y.C. is supported by the National Science Foundation of China (grant no. 11890693). M.N. acknowledges financial support from the European Union's Horizon 2020 research and innovation programme under the Marie Skłodowska-Curie grant agreement no. 707601.

References

Abazajian, K., et al. 2019, arXiv e-prints, p. arXiv:1907.04473
Ade, P., et al. 2019, JCAP, 2019, 056
Alberts, S., et al. 2014, MNRAS, 437, 437
Alberts, S., et al. 2016, ApJ, 825, 72
Bakx, T. J. L. C., et al. 2018, MNRAS, 473, 1751
Barger, A. J., Cowie, L. L., Sanders, D. B., Fulton, E., Taniguchi, Y., Sato, Y., Kawara, K., & Okuda, H. 1998, Nature, 394, 248
Barger, A. J., Cowie, L. L., Smail, I., Ivison, R. J., Blain, A. W., & Kneib, J. P. 1999, AJ, 117, 2656
Basu, K., et al. 2019, arXiv e-prints, p. arXiv:1909.01592
Baugh, C. M., Lacey, C. G., Frenk, C. S., Granato, G. L., Silva, L., Bressan, A., Benson, A. J., & Cole, S. 2005, MNRAS, 356, 1191
Benitez, N., et al. 2014, arXiv e-prints, p. arXiv:1403.5237
Bernardi, M., Shankar, F., Hyde, J. B., Mei, S., Marulli, F., & Sheth, R. K. 2010, MNRAS, 404, 2087
Bethermin, M., et al. 2020, arXiv e-prints, p. arXiv:2002.00962
Biggs, A. D., Younger, J. D., & Ivison, R. J. 2010, MNRAS, 408, 342
Blain, A. W., & Longair, M. S. 1993, MNRAS, 264, 509
Bleem, L. E., et al. 2020, ApJS, 247, 25
Bonato, M., et al. 2019, PASA, 36, e017
Boselli, A., et al. 2016, A&A, 596, A11
Bothwell, M. S., et al. 2013, MNRAS, 429, 3047
Boylan-Kolchin, M., Springel, V., White, S. D. M., Jenkins, A., & Lemson, G. 2009, MNRAS, 398, 1150
Cañameras, R., et al. 2015, A&A, 581, A105
Cañameras, R., et al. 2017, A&A, 604, A117
Cañameras, R., et al. 2018, A&A, 620, A60

Cai, Z.-Y., et al. 2013, ApJ, 768, 21
Cai, Z.-Y., Lapi, A., Bressan, A., De Zotti, G., Negrello, M., & Danese, L. 2014, ApJ, 785, 65
Cai, Z.-Y., De Zotti, G., & Bonato, M. 2020, ApJ, 891, 74
Carniani, S., et al. 2017, A&A, 605, A42
Carniani, S., et al. 2018, MNRAS, 478, 1170
Casey, C. M., et al. 2012a, ApJ, 761, 139
Casey, C. M., et al. 2012b, ApJ, 761, 140
Casey, C. M., Narayanan, D., & Cooray, A. 2014, Phys. Rep., 541, 45
Casey, C. M., et al. 2015, ApJL, 808, L33
Chapman, S. C., Blain, A. W., Smail, I., & Ivison, R. J. 2005, ApJ, 622, 772
Chen, C.-C., et al. 2016, ApJ, 831, 91
Chluba, J., et al. 2019, arXiv e-prints, p.arXiv:1909.01593
Clements, D. L., et al. 2016, MNRAS, 461, 1719
Cooke, E. A., et al. 2018, ApJ, 861, 100
Cutri, R. M., et al. 2013, Technical report, Explanatory Supplement to the AllWISE Data Release Products
Danielson, A. L. R., et al. 2017, ApJ, 840, 78
Dannerbauer, H., Lehnert, M. D., Lutz, D., Tacconi, L., Bertoldi, F., Carilli, C., Genzel, R., & Menten, K. 2002, ApJ, 573, 473
Dannerbauer, H., Lehnert, M. D., Lutz, D., Tacconi, L., Bertoldi, F., Carilli, C., Genzel, R., & Menten, K. M. 2004, ApJ, 606, 664
Dannerbauer, H., Walter, F., & Morrison, G. 2008, ApJL, 673, L127
Dannerbauer, H., et al. 2014, A&A, 570, A55
Dannerbauer, H., et al. 2019a, BAAS, 51, 293
Dannerbauer, H., Harrington, K., Daz-Sánchez, A., Iglesias-Groth, S., Rebolo, R., Genova-Santos, R. T., & Krips, M. 2019b, AJ, 158, 34
De Looze, I., et al. 2014, A&A, 568, A62
Delabrouille, J., et al. 2019, arXiv e-prints, p.arXiv:1909.01591
Dessauges-Zavadsky, M., et al. 2019, Nature Astronomy, 3, 1115
Díaz-Sanchez, A., Iglesias-Groth, S., Rebolo, R., & Dannerbauer, H. 2017, ApJL, 843, L22
Dressler, A. 1980, ApJ, 236, 351
Dudzevičiūtė, U., et al. 2020, MNRAS, 494, 3828
Dunlop, J. S., et al. 2004, MNRAS, 350, 769
Eales, S., et al. 2010, PASP, 122, 499
Flores-Cacho, I., et al. 2016, A&A, 585, A54
Franceschini, A., Toffolatti, L., Mazzei, P., Danese, L., & de Zotti, G. 1991, A&A Supp., 89, 285
Fu, H., et al. 2012, ApJ, 753, 134
Fudamoto, Y., et al. 2017, MNRAS, 472, 2028
Fujimoto, S., et al. 2019, ApJ, 887, 107
Gobat, R., et al. 2011, A&A, 526, A133
Gómez-Guijarro, C., et al. 2019, ApJ, 872, 117
Gonzalez, A. H., et al. 2019, ApJS, 240, 33
Grandis, S., Mohr, J. J., Dietrich, J. P., Bocquet, S., Saro, A., Klein, M., Paulus, M., & Capasso, R. 2019, MNRAS, 488, 2041
Gruppioni, C., et al. 2013, MNRAS, 432, 23
Gruppioni, C., et al. 2015, MNRAS, 451, 3419
Gullberg, B., et al. 2015, MNRAS, 449, 2883
Hanany, S., et al. 2019, arXiv e-prints, p.arXiv:1902.10541
Harrington, K. C., et al. 2016, MNRAS, 458, 4383
Harrington, K. C., et al. 2018, MNRAS, 474, 3866
Hashimoto, T., et al. 2018, Nature, 557, 392
Heckman, T. M., & Best P. N. 2014, ARA&A, 52, 589
Hezaveh, Y. D., et al. 2013, ApJ, 767, 132
Higuchi, R., et al. 2019, ApJ, 879, 28
Hill, R., et al. 2020, arXiv e-prints, p.arXiv:2002.11600
Hilton, M. et al., 2018, ApJS, 235, 20
Hughes, D. H., et al. 1998, Nature, 394, 241
Hung, C.-L., et al. 2016, ApJ, 826, 130
Inoue, A. K., et al. 2016, Science, 352, 1559
Ivison, R. J., Smail, I., Le Borgne, J. F., Blain, A. W., Kneib, J. P., Bezecourt, J., Kerr, T. H., & Davies, J. K. 1998, MNRAS, 298, 583
Ivison, R. J., et al. 2002, MNRAS, 337, 1
Ivison, R. J., et al. 2013, ApJ, 772, 137
Ivison, R. J., Page, M. J., Cirasuolo, M., Harrison, C. M., Mainieri, V., Arumugam, V., & Dudzevičiūtė, U. 2019, MNRAS, p. 2100
Jones, G. C., Maiolino, R., Caselli, P., & Carniani, S. 2019, A&A, 632, L7
Kato, Y., et al. 2016, MNRAS, 460, 3861
Kauffmann, G., White, S. D. M., Heckman, T. M., Ménard, B., Brinchmann, J., Charlot, S., Tremonti, C., & Brinkmann, J. 2004, MNRAS, 353, 713
Kaviani, A., Haehnelt, M. G., & Kauffmann, G. 2003, MNRAS, 340, 739
Kennicutt, R. C., & Evans, N. J. 2012, ARA&A, 50, 531
King, A., & Pounds, K. 2015, ARA&A, 53, 115
Klein, M., et al. 2019, MNRAS, 488, 739
Kneissl, R., et al. 2019, A&A, 625, A96
Kravtsov, A. V., & Borgani S. 2012, ARA&A, 50, 353
Kubo, M., et al. 2019, ApJ, 887, 214
LSST Science Collaboration 2009, arXiv e-prints, p.arXiv:0912.0201
Lacaille, K. M., et al. 2019, MNRAS, 488, 1790
Laporte, N., et al. 2017, ApJL, 837, L21
Laureijs, R., et al. 2011, arXiv e-prints, p.arXiv:11http://dx.doi.org/10.3193
Lemaux, B. C., et al. 2019, MNRAS, 490, 1231
Lima, M., Jain, B., & Devlin, M. 2010, MNRAS, 406, 2352
Lupu, R. E., et al. 2012, ApJ, 757, 135
Lutz, D. 2014, ARA&A, 52, 373
Magnelli, B., et al. 2013, A&A, 553, A132
Mancuso, C., et al. 2015, ApJ, 810, 72
Massardi, M., et al. 2018, A&A, 610, A53
Meixner, M., et al. 2019, arXiv e-prints, p.arXiv:1912.06213
Miller, T. B., et al. 2018, Nature, 556, 469
Mocanu, L. M., et al. 2013, ApJ, 779, 61
Nantais, J. B., et al. 2017, MNRAS, 465, L104
Nayyeri, H., et al. 2016, ApJ, 823, 17
Negrello, M., González-Nuevo, J., Magliocchetti, M., Moscardini, L., De Zotti, G., Toffolatti, L., & Danese, L. 2005, MNRAS, 358, 869
Negrello, M., Perrotta, F., González-Nuevo, J., Silva, L., de Zotti, G., Granato, G. L., Baccigalupi, C., & Danese, L. 2007, MNRAS, 377, 1557
Negrello, M., et al. 2010, Science, 330, 800
Negrello, M., et al. 2014, MNRAS, 440, 1999
Negrello, M. et al. 2017a, MNRAS, 465, 3558
Negrello, M., et al. 2017b, MNRAS, 470, 2253
Neri, R., et al. 2020, A&A, 635, A7
Nesvadba, N. P. H., Cañameras, R., Kneissl, R., Koenig, S., Yang, C., Le Floc'h, E., Omont, A., & Scott, D. 2019, A&A, 624, A23
Nguyen, H. T., et al. 2010, A&A, 518, L5
Niemi, S.-M., Somerville, R. S., Ferguson, H. C., Huang, K.-H., Lotz, J., & Koekemoer, A. M. 2012, MNRAS, 421, 1539
Oguri, M., et al. 2018, PASJ, 70, S20
Oliver, S. J., et al. 2012, MNRAS, 424, 1614
Oteo, I., et al. 2018, ApJ, 856, 72
Overzier, R. A. 2016, , 24, 14
Overzier, R., & Kashikawa, N. 2019, BAAS, 51, 180
Paciga, G., Scott, D., & Chapin, E. L. 2009, MNRAS, 395, 1153
Papadopoulos, P. P., Thi, W.-F., Miniati, F., & Viti, S. 2011, MNRAS, 414, 1705
Perrotta, F., Baccigalupi, C., Bartelmann, M., De Zotti, G., & Granato, G. L. 2002, MNRAS, 329, 445
Planck Collaboration Int. XXVII 2015, A&A, 582, A30
Planck Collaboration Int. XXXIX 2016, A&A, 596, A100
Planck Collaboration VI 2018, arXiv e-prints, p.arXiv:1807.06209
Planck Collaboration XXIV 2016, A&A, 594, A24
Planck Collaboration XXVII 2016, A&A, 594, A27
Pope, A., Borys, C., Scott, D., Conselice, C., Dickinson, M., & Mobasher, B. 2005, MNRAS, 358, 149
Pope, A., et al. 2006, MNRAS, 370, 1185
Prandoni, I., & Seymour, N. 2015, in Advancing Astrophysics with the Square Kilometre Array (AASKA14), 67 (arXiv:1412.6512)
Riechers, D. A., et al. 2013, Nature, 496, 329
Rodríguez-Muñoz, L., et al. 2019, MNRAS, 485, 586
Sartoris, B., et al. 2016, MNRAS, 459, 1764
Schaerer, D., et al. 2020, arXiv e-prints, p.arXiv:2002.00979

https://doi.org/10.1017/pasa.2020.16 Published online by Cambridge University Press

Sheth, R. K., & Tormen, G. 1999, MNRAS, 308, 119
Sheth, R. K., Mo, H. J., & Tormen, G. 2001, MNRAS, 323, 1
Silva, M. B., et al. 2019, arXiv e-prints, p.arXiv:1908.07533
Smail, I., Ivison, R. J., & Blain, A. W. 1997, ApJL, 490, L5
Smit, R., et al. 2018, Nature, 553, 178
Somerville, R. S., Gilmore, R. C., Primack, J. R., & Domnguez, A. 2012, MNRAS, 423, 1992
Spergel, D., et al. 2015, arXiv e-prints, p.arXiv:1503.03757
Spilker, J. S., et al. 2018, Science, 361, 1016
Springel, V., et al. 2005, Nature, 435, 629
Sridhar, S., Maurogordato, S., Benoist, C., Cappi, A., & Marulli, F. 2017, A&A, 600, A32
Stacey, G. J., Hailey-Dunsheath, S., Ferkinhoff, C., Nikola, T., Parshley, S. C., Benford, D. J., Staguhn, J. G., & Fiolet, N. 2010, ApJ, 724, 957
Sutter, J. 2019, in Linking Galaxies from the Epoch of Initial Star Formation to Today, 4 (arXiv:1910.05416), doi:10.5281/zenodo.2635203
Swinbank, A. M., Smail, I., Chapman, S. C., Blain, A. W., Ivison, R. J., & Keel, W. C. 2004, ApJ, 617, 64
Symeonidis, M. 2017, MNRAS, 465, 1401
Symeonidis, M., Giblin, B. M., Page, M. J., Pearson, C., Bendo, G., Seymour, N., & Oliver, S. J. 2016, MNRAS, 459, 257
Tamura, Y., et al. 2019, ApJ, 874, 27
Toshikawa, J., et al. 2018, PASJ, 70, S12
Umehata, H., et al. 2019, Science, 366, 97
Valiante, E., et al. 2016, MNRAS, 462, 3146
Venemans, B. P., et al. 2007, A&A, 461, 823
Vieira, J. D., et al. 2013, Nature, 495, 344
Viero, M. P., et al. 2014, ApJS, 210, 22
Wagner, C. R., et al. 2017, ApJ, 834, 53
Walter, F., et al. 2012, Nature, 486, 233
Wang, J., et al. 2011, MNRAS, 413, 1373
Wang, T., et al. 2016, ApJ, 828, 56
Wang, T., et al. 2019a, Nature, 572, 211
Wang, L., Pearson, W. J., Cowley, W., Trayford, J. W., Béthermin, M., Gruppioni, C., Hurley, P., & Michałowski, M. J. 2019b, A&A, 624, A98
Wardlow, J. L., et al. 2013, ApJ, 762, 59
Weiss, A., et al. 2013, ApJ, 767, 88
Wen, Z. L., & Han J. L. 2018, MNRAS, 481, 4158
Williams, C. C., et al. 2019, ApJ, 884, 154
Wright, E. L., et al. 2010, AJ, 140, 1868
Yang, C., et al. 2017, A&A, 608, A144
Younger, J. D., et al. 2007, ApJ, 671, 1531
Zhang, Z.-Y., et al. 2018a, MNRAS, 481, 59
Zhang, Z.-Y., Romano, D., Ivison, R. J., Papadopoulos, P. P., & Matteucci, F. 2018b, Nature, 558, 260
de Haan T., et al. 2016, ApJ, 832, 95

https://doi.org/10.1017/pasa.2020.16 Published online by Cambridge University Press